Dual-Frequency, Harmonic, Magnetically Insulated Line Oscillator

Ryan A. Revolinsky, *Graduate Student Member, IEEE*, Emma N. Guerin, *Graduate Student Member, IEEE*, Stephen V. Langellotti, *Member, IEEE*, Christopher J. Swenson, *Graduate Student Member, IEEE*, Levi I. Welch, *Student Member, IEEE*, Drew A. Packard, *Member, IEEE*, Nicholas M. Jordan, *Senior Member, IEEE*, Y. Y. Lau, *Fellow, IEEE*, and Ronald M. Gilgenbach, *Life Fellow, IEEE*

***Abstract*— Magnetically insulated line oscillators (MILOs) are crossed-field devices which generate a self-induced azimuthal magnetic field via an axial current. This negates the need for external magnets, potentially increasing overall system efficiency at the expense of reduced device efficiency. This article reports the design, simulation, and experimental demonstration of a dual-frequency, harmonic MILO (HMILO), which is composed of two sequential slow wave structures (SWSs) tuned for oscillation at different frequencies, each paired with a set of choke cavities and insulated by the self-generated magnetic field of the common cathode. The two SWSs—designed for operation in *L*- and *S*-bands at 1 and 2 GHz, respectively—were tested independently before the HMILO experiments. Results for the *L*-band MILO (L-MILO) were reported previously by Packard. In the experiments reported here, the isolated *S*-band MILO (S-MILO) produced 1.1 ± 0.7 MW of output power at 2.076 ± 0.005 GHz, when supplied with 207 kV and 7.3 kA from the MELBA-C generator. Ultimately, when implementing two separate extractor configurations, the HMILO produced 12.7 ± 7.6 MW at 0.984 ± 0.013 GHz and 3.2 ± 1.5 MW at 2.074 ± 0.003 GHz. These results are compared against simulated performance in the particle-in-cell (PIC) codes CST and improved concurrent electromagnetic PIC (ICEPIC).**

***Index Terms*— Brillouin flow, crossed-field, harmonic, high power microwaves (HPMs), magnetically insulated line oscillator (MILO), Marx-generators, pulsed power, radio frequency (RF), slow wave structure (SWS).**

I. Introduction

HIGH-POWER microwaves (HPMs), focusing on a crossed field architecture, are generated through pulsed power (single or rep-rated pulses) or through continuous drive, and are of increasing interest due to their applications in communications, radar, plasma heating, commercial heating, medical treatment, plasma processing, and defense. Advances in HPM theory and practice benefit a variety of fields, including fusion, space exploration, and astrophysics [1], [2], [3], [4].

Utilization of HPM devices dates to Albert Hull's magnetic valve design from 1921, which was developed to bypass a popular triode patent [5], [6], [7]. Hull inadvertently created what is now considered to be the first magnetron. Magnetrons became popularized in World War II by the Tizard Mission with their usage in the novel radar technology of the 1940s [7].

Within the last 30 years, research on a novel HPM technology called the magnetically insulated line oscillator (MILO) has become widespread, which shares some device similarities to the magnetron. The MILO device was patented by Clark et al. [8] and Bacon et al. [9] in 1987, with intended uses in fusion plasma heating, charged particle acceleration, and directed energy sources. The primary difference between MILOs and magnetrons is the requirement of an external magnetic field for a magnetron to achieve insulation of the electron hub. The magnetic field at which magnetic insulation is achieved is known as the Hull cutoff (HC) condition. The MILO, in contrast, produces self-magnetic insulation via axial flow of current along its cathode, which is unique among most crossed-field devices.

In this work, we designed, simulated, and experimentally validated a high impedance, dual-frequency, harmonic MILO (HMILO) driven by a single source. The two frequency bands selected for the HMILO are the *L*-band (1 GHz) and the *S*-band (2 GHz). Nonharmonic dual-frequency MILOs, such as the BFMILO (≈1.3 and ≈1.5 GHz) have been demonstrated previously [10]. For logical design progression, an *L*-band MILO (L-MILO) was developed and tested [11], followed by an *S*-band MILO (S-MILO), and culminating with the combination of the two slow wave structures (SWSs) in the HMILO. This harmonic design progression follows a related experiment performed by Packard et al. [12] on harmonic recirculating planar magnetrons.

Section II provides a brief background of the novel Brillouin flow solutions along with the application of such solutions for MILO design. Section III discusses simulation and

Manuscript received 22 December 2022; revised 28 March 2023; accepted 27 May 2023. This work was supported in part by the Office of Naval Research (ONR) under Grant N00014-19-1-2262. The review of this article was arranged by Senior Editor J. G. Leopold. *(Corresponding author: Ryan A. Revolinsky.)*

Ryan A. Revolinsky, Emma N. Guerin, Christopher J. Swenson, Levi I. Welch, Nicholas M. Jordan, Y. Y. Lau, and Ronald M. Gilgenbach are with the Department of Nuclear Engineering and Radiological Sciences (NERS), University of Michigan, Ann Arbor, MI 48109 USA (e-mail: revolins@umich.edu).

Stephen V. Langellotti was with the Department of Nuclear Engineering and Radiological Sciences (NERS), University of Michigan, Ann Arbor, MI 48109 USA. He is now with Northrop Grumman Mission Systems, Rolling Meadows, IL 60008 USA.

Drew A. Packard was with the Department of Nuclear Engineering and Radiological Sciences (NERS), University of Michigan, Ann Arbor, MI 48109 USA. He is now with the RF Technology Group, General Atomics, San Diego, CA 92121 USA.

Color versions of one or more figures in this article are available at https://doi.org/10.1109/TPS.2023.3285509.

Digital Object Identifier 10.1109/TPS.2023.3285509

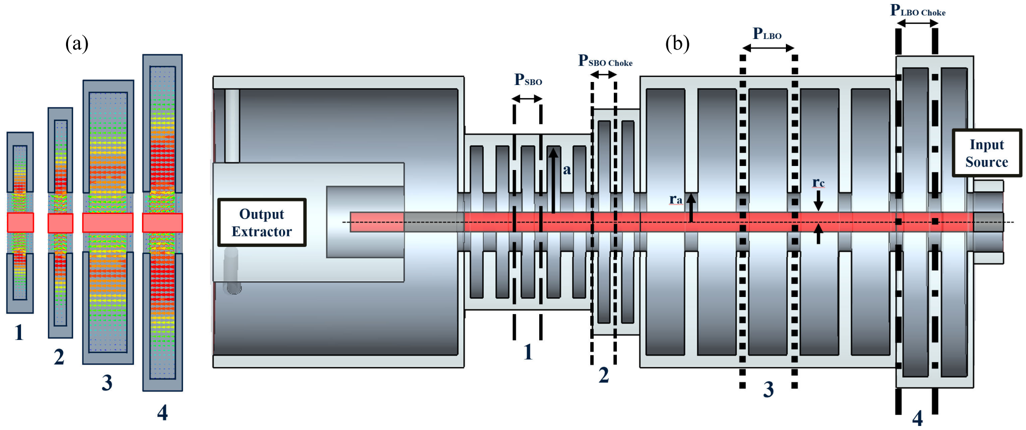

Fig. 1. (a) Eigenmode simulation models for the individual unit cells of: 1–S-band cavity, 2–S-band choke, 3–L-band cavity, and 4–L-band choke with electric field vectors at zero phase. (b) Model used for the finite cavity simulations of the whole MILO structure.

design choices of the S-MILO and HMILO. Experimental setup of each MILO is then discussed in Section IV. Results of the experiments are presented and analyzed in Section V, then directly compared to the novel Brillouin flow theory in Section VI. The conclusion is given in Section VII.

II. Theory

The Brillouin flow solution for a cylindrical MILO was recently derived explicitly, in closed form, by Lau et al. [13]. This theory is formulated in terms of two parameters, the anode–cathode (AK) gap voltage (V_a) and the magnetic flux per unit axial length within the AK gap (A_a). These two quantities are normalized as

$$\bar{V}_a = V_a/V_s = V_a e/(mc^2) \tag{1}$$

$$\bar{A}_a = A_a/A_s = A_a e/(mc). \tag{2}$$

The gap voltage yields

$$\gamma_a = \bar{V}_a + 1 = \frac{1}{\sqrt{1-\beta_a^2}} \tag{3}$$

$$\bar{A}_a^{\min} = \gamma_a \beta_a \tag{4}$$

where (4) gives the minimum normalized magnetic flux required for magnetic insulation at the given gap voltage, V_a. Thus, the quantity

$$f = \bar{A}_a/\bar{A}_a^{\min} \tag{5}$$

then denotes the degree of magnetic insulation at a given magnetic flux, and f is roughly equal to the ratio of the magnetic field to the HC magnetic field [13]. Magnetic insulation requires $f > 1$. The two parameters, V_a and f, then completely specify the Brillouin flow profile including the Brillouin flow hub height, flow velocity at the top of the Brillouin hub, the electron current carried within the Brillouin hub, and the anode (input) current, I_a, that is required to yield this value of f. Packard et al. [11] used this Brillouin flow theory to design and to interpret their MILO experiment operating at 240 kV and 10 kA at L-band. Here, we shall use a similar procedure to design the S-band oscillator (SBO), assuming that the L-band oscillator (LBO) and SBO are isolated from each other.

For an SBO operating at the π-mode of a SWS with a periodicity (pitch) P, at a resonant frequency, f_{res}, its phase velocity is given by

$$v_{\text{ph}} = \frac{\omega}{k} = 2 f_{\text{res}} P. \tag{6}$$

Alternatively, specifying the frequency and the operating π-mode's phase velocity (which is bounded by the Brillouin flow velocity at the top of the Brillouin hub), the pitch P is given by

$$P = \frac{\beta_{\text{ph}} c}{2 f_{\text{res}}}. \tag{7}$$

The anode and cathode radius for the SBO were designed using the same procedure outlined by Packard et al. [11] for the L-band. A new formula on the degree of magnetic insulation at Buneman–Hartree (BH) condition is presented in the Appendix.

III. Simulation and Design

An intermediate step toward the HMILO was demonstration of successful, independent L-MILO and S-MILO. The L-MILO was already covered in-depth by Packard et al. [11], and the LBO portion of the HMILO utilizes the same geometric dimensions as Packard's L-MILO. Therefore, design of only the S-MILO—and subsequently the SBO section of the HMILO—was required, with the L-MILO restricting some design scope.

As mentioned in Section I, target frequencies for the HMILO (and independent oscillators) are 1 GHz (LBO) and 2 GHz (SBO). As the SBO and LBO in the HMILO will be driven by the same pulsed power source, the current and voltage values observed in L-MILO experiments were used to guide the design. The source parameters used for dimensioning the (independent SBO) S-MILO were 250 kV and 10 kA [11]. Applying the theory, the radius of the cathode (r_c) was selected to be 8 mm, which gives the inner anode radius (r_a) of 25 mm, as shown in Fig. 1(b). These two radii are very similar to those reported for the L-MILO by Packard et al. [11]. This

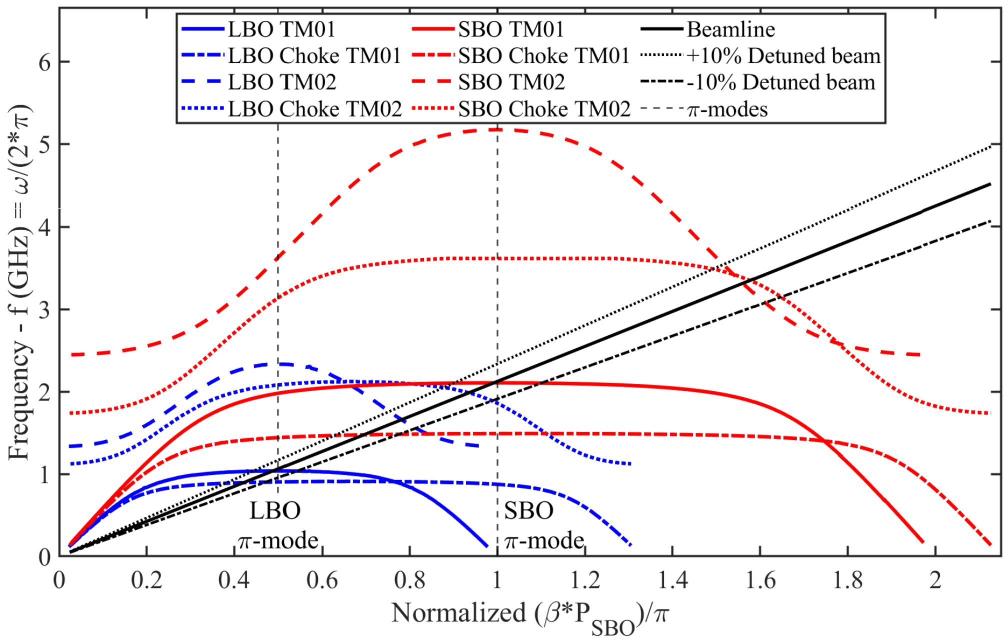

Fig. 2. Dispersion relation diagram of individual unit cell cavities of each frequency band for the fundamental TM_{01} mode and the next transverse magnetic mode, TM_{02}, with an electron beamline and phase velocity of $0.287c$. Hybrid electric and magnetic modes are not depicted.

simplifies manufacturing and assembly of the HMILO by keeping the anode and cathode radius the same. The radius of the outer anode (a) was calculated to be 63.75 mm (from cathode surface to the back of the vane, vane depth). The phase velocity (β) was set to 0.287 to align with the L-MILO's design (see Fig. 2), which is identical to Packard et al. [11]. Therefore, the circuit pitch for the S-MILO SWS becomes 21.5 mm, according to (7).

Multiple simulation methods and tools were implemented alongside the analytic theory to design a dual-band HMILO. The main tools include: a unit cell approach using high frequency electromagnetic simulation software (HFSS from ANSYS) [14], an eigenmode solver for fast dispersion diagrams, a finite cavity method using CST Microwave Studio's eigenmode solver for overall cold system design, and two particle-in-cell (PIC) codes for radio frequency (RF) e-beam (hot) system design. The PIC codes used are CST-Particle Studio (CST-PS) and improved concurrent electromagnetic PIC (ICEPIC) [15], [16], [17], [20].

A. HFSS Unit Cell

Initial operating parameters of both MILOs which were selected and determined to be feasible according to the theory. Unit cell simulation method was then employed in HFSS using hexahedral meshing and perfect electrical conductor boundaries to tune and improve the MILO design [18]. The unit cell method is a process of focusing in on a single pitch-length of a SWS of interest, forming a model of a single cavity [see Fig. 1(a)]. With this single cavity, one then applies a master/slave boundary condition to openings on each side of the SWS; this treats the system as an infinite structure along its axis [19]. Phase change then must be parameterized through at least one full period which mimics a transverse RF electric field wave propagating through the structure.

These HFSS unit cells provide fast and accurate cold tests and dispersion relation diagrams of each SWS [20]. In this case, the SWS cavities simulated are: 1–*S*-band cavity (SBO), 2–*S*-band choke cavity (SBO Choke), 3–*L*-band cavity (LBO), and 4–*L*-band choke cavity (LBO Choke), which are displayed in Fig. 1(a). The electric field is depicted for each unit cell at zero phase, representing fundamental mode operation. Overall placement of each unit cell in the full HMILO model is shown in Fig. 1(b).

Results of the unit cell simulations on individual cavities [see Fig. 1(a)] are presented in Fig. 2, which is a dispersion diagram displaying the frequency as a function of a normalized phase propagation constant (β) [21], [22]. The phase propagation constant is multiplied by the pitch of the SBO cavity (P_{SBO}) and divided by π, simplifying the x-axis. The dispersion diagram is normalized to the SBO π-mode, in solid red, so the LBO π-mode, in solid blue, corresponds to a value of 0.5 on the horizontal axis. Both the fundamental mode (TM_{01}) and next higher order transverse magnetic mode (TM_{02}) are plotted for all four-unit cells, along with the corresponding beamline that interacts with the SBO and LBO cavity's π-modes simultaneously, allowing spoke formation to occur synchronously in both structures. The phase velocity of the beamline for dual π-mode operation is $0.287c$. Inclusion of 10% detuned beamlines (black dotted lines) in Fig. 2 demonstrate the spread in the electron's axial beam velocities which is intrinsic in the Brillouin flow model. The next higher order modes that are supported by the LBO and SBO are hybrid electric and magnetic modes which are not represented in Fig. 2 [23], [24], [25]. The LBO has two hybrid modes (HEM_{11}, HEM_{21}), and the SBO has three hybrid modes (HEM_{11}, HEM_{21}, HEM_{31}), between the TM_{01} and TM_{02} mode for the primary SWSs. For all given frequencies in the dispersion relation, evaluating each band individually, no interaction

TABLE I

SUMMARY OF HFSS UNIT CELL EIGENMODE SIMULATIONS

Unit Cell				
Mode	**Fundamental - TM_{01} (GHz)**			
	LBO	**LBO Choke**	**SBO**	**SBO Choke**
π	1.037	0.903	2.107	1.491
$5\pi/6$	1.03	0.894	2.098	1.485
$2\pi/3$	1.019	0.887	2.086	1.48
$\pi/2$	0.928	0.828	1.98	1.44
Mode	**1st Higher Order - HEM_{11} (GHz)**			
	LBO	**LBO Choke**	**SBO**	**SBO Choke**
π	1.595	1.375	2.634	1.994
Mode	**2nd Higher Order - HEM_{21} (GHz)**			
	LBO	**LBO Choke**	**SBO**	**SBO Choke**
π	2.211	1.906	3.679	2.845
Mode	**3rd Higher Order - HEM_{31} (GHz)**			
	LBO	**LBO Choke**	**SBO**	**SBO Choke**
π	N/A	N/A	4.745	N/A
Mode	**Next Transverse Magnetic - TM_{02} (GHz)**			
	LBO	**LBO Choke**	**SBO**	**SBO Choke**
π	2.333	2.08	5.174	3.616
$5\pi/6$	2.272	2.01	5.04	3.601
$2\pi/3$	2.188	1.95	4.831	3.563
$\pi/2$	1.77	1.592	3.628	3.121

occurred between the fundamental mode (TM_{01}), and the all the higher order modes (HEM_{11}, HEM_{21}, HEM_{31}, and TM_{02}), in what is often called the forbidden region of operation [26]. If a higher order mode does occur, it will not share the same frequency with the fundamental mode of the structure.

Selection of the ratio of vane to cavity width in terms of the pitch was tuned with unit cell simulation and was selected to be 50%, meaning both the cavity and vane thicknesses are 10.75 mm thick [27], [28], [29].

Table I lists key modes extracted from the dispersion relations in Fig. 2, which exhibit large separation of operational frequency between $3\pi/5$, $2\pi/5$, and $\pi/5$ modes for the fundamental wave mode in the primary SWS cavities (LBO and SBO). Minor separation was noted for the displayed three primary modes (flat top dispersion). The next higher order hybrid electric and magnetic modes at π-mode operation are also provided for convenience. Considerable detuning of the beam would be required to promote non-π-mode excitation in the SWS.

B. CST Finite Model

With functional unit cells for the SBO and the LBO, each with a cavity and choke, a full finite cavity model was then generated with a merging of five cavities and two chokes on *L*-band and *S*-band. This forms the initial CST eigenmode solver setup for a finite cavity model of the HMILO in Fig. 1(b). This model used a tetrahedral mesh and perfect electrical conductor for the eigenmode simulation. Selection of five cavities and two chokes achieved optimal operation based on length restrictions, maximized oscillation, and mode optimization. The chokes cavities are evanescent to the SWS's π-mode wave causing a reflection of backwards propagating waves [30]. Design and placement of the extractor,

TABLE II

CST FINITE CAVITY TABULATED DATA OF SBO AND LBO SWS CAVITIES

Finite Cavity		
Parameters	**SBO**	**LBO**
Modes	π - TM_{01}	π - TM_{01}
Frequency (GHz)	2.065	1.027
Total Q	4350	828.2

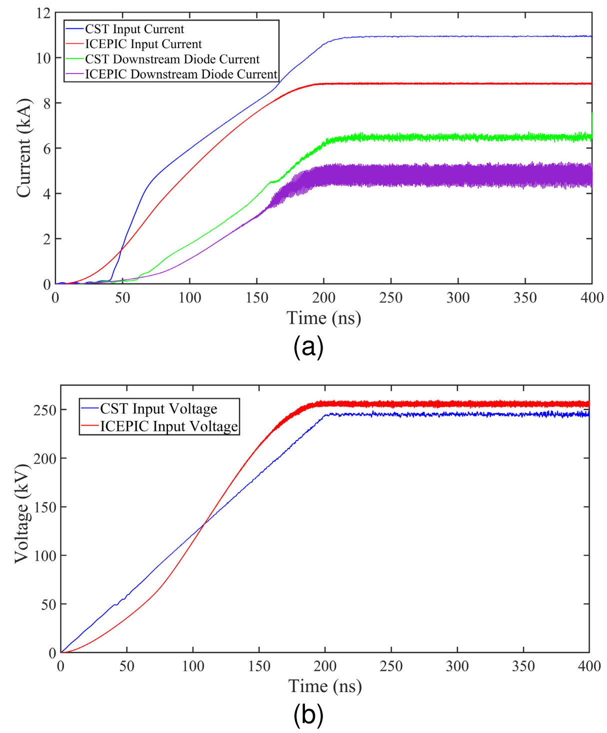

Fig. 3. PIC simulation of currents and voltages from ICEPIC and CST-PS. (a) Input and DSD current. (b) Input voltage.

beam-dump, and downstream diode (DSD) are covered in Section IV [26]. Results of the finite cavity simulation are tabulated in Table II for the fundamental wave mode at π-mode for only the finite five cavity SWS of the SBO and LBO. All of the higher order modes frequency operation at π mode agree with unit cell model from Table I.

C. PIC Simulation

Computationally expensive and time-consuming CST-PS PIC and ICEPIC simulations, which was also used previously for the L-MILO [11], likewise enabled fine tuning of the HMILO. They gave preliminary insight into the HMILO operation demonstrated in Figs. 3–5. The CST-PS and ICEPIC simulation models were the same as the model used for the finite cavity eigenmode solver, depicted in Fig. 1. While simulations of the S-MILO were conducted, for the sake of brevity, only the HMILO PIC simulations are presented here. Both simulations used approximately the same number of total hexahedral mesh cells, as determined by convergence studies of the output power as described by Greenwood [31].

As shown in Fig. 3(b), both PIC simulations applied a steady-state input voltage of 250 kV with a 200 ns rise time,

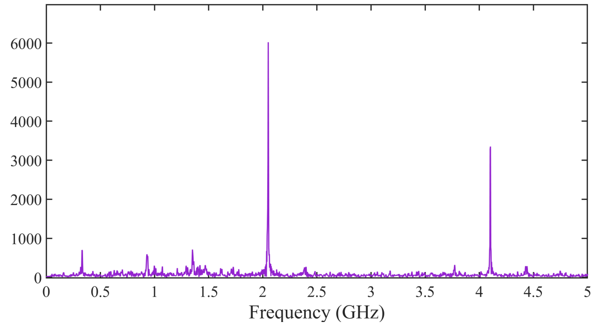

(a)

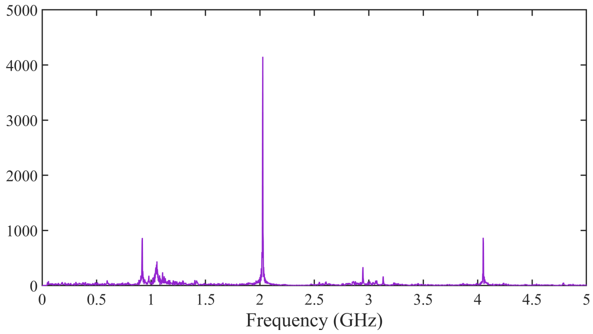

(b)

Fig. 4. FFTs of the PIC simulation RF output voltage from (a) CST (dominant frequency = 2.05 GHz) and (b) ICEPIC (dominant frequency = 2.026 GHz). CST simulations produced very weak L-band oscillations, relative to S-band.

the resulting input and DSD currents are presented in Fig. 3(a). The input current is measured at the input port of the MILO, while the DSD current is measured between the last SBO cavity and beam-dump. Steady state input and DSD currents were 11 and 7 kA for CST-PS, and 9 and 5 kA for ICEPIC, respectively. This deviation in current between simulations can be attributed primarily to mesh and electron emission density in the DSD regions.

Fast Fourier transforms (FFTs) obtained from the two PIC codes (see Fig. 4), showed some discrepancies in both the S-band frequency and L-band amplitude. The S-band frequency was dominant at 2.05 and 2.026 GHz for CST-PS and ICEPIC, respectively. Relative to the S-band, the CST-PS FFT demonstrates very little oscillation of the L-band frequency target, while the ICEPIC simulations exhibit more pronounced L-band signals. The low L-band FFT response is correlated with unmatched total quality factors (Total Q, see Table II) of the L- and S-bands structures, which suggests that the S-band would out-compete the L-band in the TM_{01}, π-mode in simulation. Placement of the S-band structure in series between the L-band structure and the extractor could cause an attenuation/coupling issue in the PIC simulation. This reduced L-band behavior is not observed in experiment. A strong frequency response at 4 GHz in both CST and ICEPIC is observed in the FFTs, alluding to harmonic behavior of the S-band frequency in the PIC simulations.

Output power over the 250 kV input voltage time is shown in Fig. 5. Generation of the output power trace was achieved using the electric field signal at the output extractor face, via a Poynting vector power calculation [29]. Steady-state

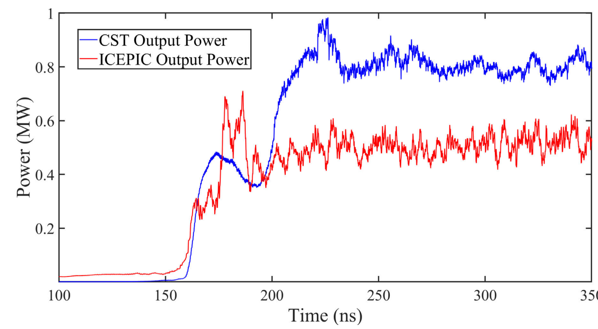

Fig. 5. PIC simulation of output power from ICEPIC and CST.

output power from CST-PS PIC is 0.8 MW and ICEPIC is 0.5 MW depicted in Fig. 5. The variance can be attributed to difference in input and DSD current between the PIC codes; CST's currents are 25% greater than ICEPIC. Accounting for the variance of input current *fair agreement* between the PIC simulation is demonstrated, as was observed by Andreev et al. [32]. The number of cavities and chokes for each SWS was optimized for peak output power from both PIC codes.

IV. Experimental Configuration

As was previously described two MILO experiments were investigated, one is the S-MILO configuration shown in Fig. 6, and the other is the HMILO configuration with both L-band and S-band SWSs depicted in Fig. 7. Both these configurations are driven by the Michigan Electron Long Beam Accelerator with Ceramic insulating stack (MELBA-C) [33]. MELBA-C is a Marx–Abramyan generator with a load-dependent output of 200–300 kV and 1–10 kA for 200–500 ns. Roughing vacuum was achieved with a scroll pump down to 10^{-3} torr scale, enabling the use of a cryogenic pump which attained low 10^{-6} torr scale.

A. S-MILO Setup

The experimental setup of the S-MILO is shown in Fig. 6. The MELBA output, and MILO input, is on the right-hand side of the figure. The cathode is made of 303 stainless steel and is wrapped in a sleeve of red velvet. While our L-MILO varied the cathode radius in the beam dump [11], the S-MILO uses a uniform cathode radius, r_c, of 8 mm (7 mm without the velvet). The cathode and a graphite beam dump comprise the DSD. This gap is adjusted by varying the cathode length, which changes the axial current and, thus, the magnetic field generated. The beam dump is grounded to the chamber through three azimuthally spaced quarter-wave stubs, which are placed at a set axial distance to pass the extracted RF. A tapered extractor, made of 6061 aluminum, gradually converts the 10 cm diameter beam dump to the 1.9 cm diameter inner conductor of the WR340 distributed field adapter (DFA340). The DFA340 converts from the TM_{01} coaxial mode of the extraction taper to the TE_{10} mode of the WR340 waveguide [34], where the RF output subsequently passes through a waveguide window, is measured by a calibrated directional coupler, and is absorbed by the load.

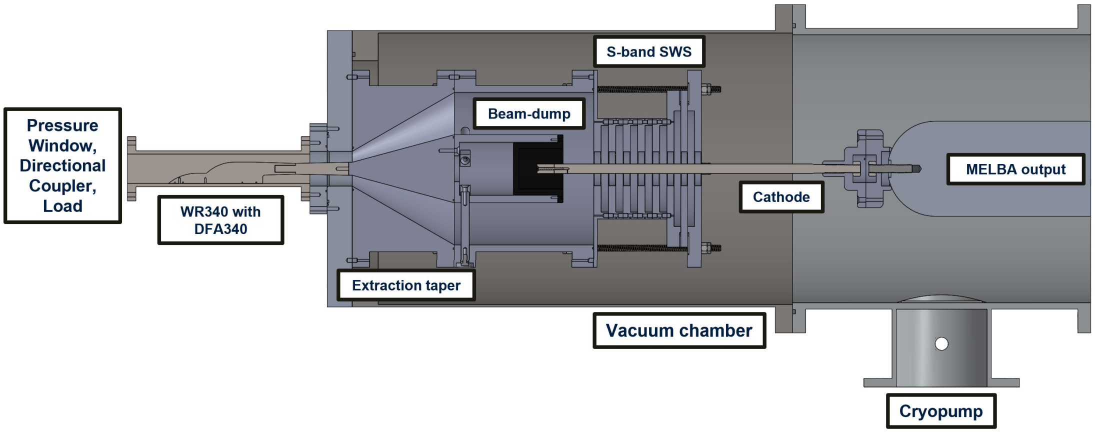

Fig. 6. CAD model/experimental setup of the S-MILO with supporting hardware. The adjustable radius tip of the *S*-band cathode forms the DSD, positioned in the beam-dump.

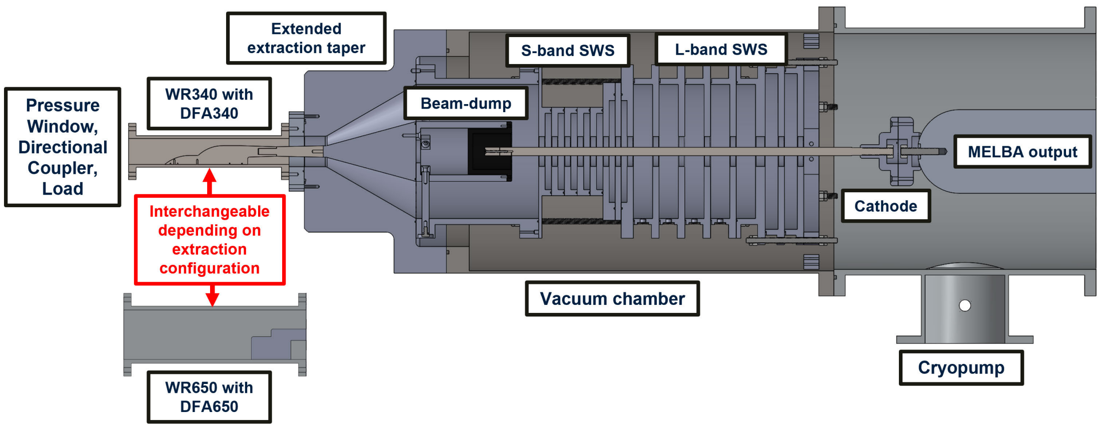

Fig. 7. CAD model/experimental setup of HMILO with supporting hardware.

From the directional coupler the RF signal is attenuated and split, where the first split RF signal is used for direct waveform capture via an oscilloscope (Agilent 54855A), and the other split RF signal is sent to diodes (Agilent 8472B) before being processed by a separate oscilloscope for power measurements (Tektronix TDS 3054B).

The *S*-band SWS, shown in the middle of Fig. 6 is also made of 303 stainless steel, see Section III for the geometric dimensions. The whole assembly is aligned with dowels and clamped together with six stainless steel rods.

B. HMILO Setup

The experimental setup for the HMILO is provided in Fig. 7 and follows the S-MILO configuration with a few changes: the addition of an *L*-band SWS and choke cavities, a lengthened cathode to accommodate the extended SWSs, an external taper to allow packaging of all the cavities in the vacuum chamber, and the interchangeable DFA extractors. The DFA340 and DFA650 have optimal transmission bands of 1.77–2.15 GHz and 0.94–1.02 GHz, respectively, with S_{21} between −0.2 and −0.02 dB [26], [34]. Consequently, neither mode converter is capable of handling the full frequency range of the HMILO, and they must be swapped between shots to properly measure the full range of frequencies emitted by the HMILO.

V. Experimental Results

Three different sets of experimental results are demonstrated in this section from the two different experimental configurations presented in Section IV. The first dataset is from the S-MILO configuration, and the other two datasets are from the HMILO experimental configuration. These two datasets from the HMILO configuration were collected using the DFA340 or DFA650, and will be referred to as the HMILO-S and HMILO-L, respectively. For the HMILO-L, a 0.9–1.1 GHz bandpass filter was added immediately following the directional coupler. This filter rejected the signal produced by the SBO which was outside the operating band of the directional coupler and could not produce calibrated power measurements.

A. S-MILO Results

A representative shot from the 55-shot S-MILO series is provided in Fig. 8. This demonstrates the voltage, current, power, impedance, and frequency from the S-MILO validating its operation. The FFT and time frequency analysis (TFA) indicate most of the output power occurs at 2.074 GHz from 675 to 775 ns.

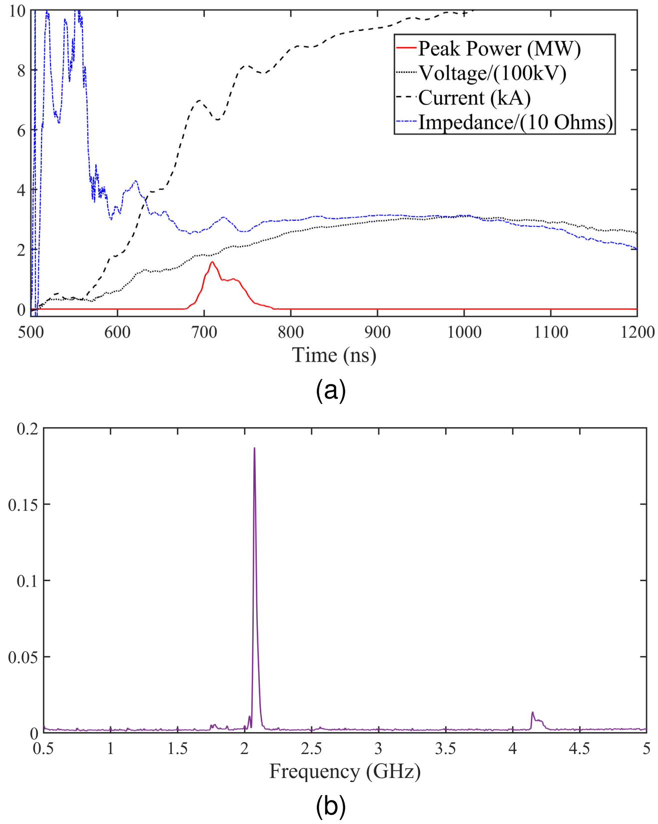

Fig. 8. Experimental S-MILO data from shot 18 492. (a) Voltage, current, power, and impedance with maximum output power of 1.6 MW at 710 ns. (b) Fourier transform of the RF signal with a dominant frequency of 2.074 GHz.

B. HMILO Results

Similar to the S-MILO data in Fig. 8, nominal HMILO results are demonstrated in Fig. 9 for each extractor style. Fig. 9(a) provides driver voltage, input current, load impedance, and output power for shot 18 695, which was a representative shot from a 25-shot series utilizing the HMILO-S extractor configuration. As Fig. 9(b) shows, the dominant frequency is 2.074 GHz, with oscillations from 800 to 900 ns. Fig. 9(c) shows the operational behavior of shot 18 734 from the 17-shot series. This was nominally the same as the shot in Fig. 9(a), but the extraction system was changed to the HMILO-L configuration to make calibrated *L*-band power measurements. These *L*-band signals are plotted in Fig. 9(d), where we see the dominant frequency is 0.985 GHz with the highest output power occurring from 775 to 875 ns.

Fig. 10 presents a combination of the FFTs from each HMILO extraction configuration. This implies dual-band frequency operation of the HMILO driven by a single source, in general consistent with the theory, design, and simulations of both the S-MILO and HMILO. Agreement between experiment and eigenmode simulations (unit cell and finite cavity) is also demonstrated, which suggests that both SWSs ran in the intended fundamental TM_{01} mode. These separate FFTs were generated using the two separate extractors referenced in Section IV-B and the beginning of Section V. The first extractor, HMILO-S, produced the SBO extracted FFT, while the second extractor, HMILO-L, produced the LBO filtered and extracted FFT.

TABLE III
SUMMARY OF RESULTS FOR EACH MILO CONFIGURATION

Metrics	S-MILO	HMILO-S	HMILO-L
Output Power (MW)	1.1 ± 0.7	3.2 ± 1.5	12.7 ± 7.6
Voltage (kV)	207 ± 31	238 ± 19	256 ± 17
Current (kA)	7.3 ± 0.9	8.6 ± 1.3	9.9 ± 0.7
Impedance (Ohms)	28.2 ± 4.8	27.9 ± 4.0	25.9 ± 1.6
Dominant Frequency (GHz)	2.076 ± 0.005	2.074 ± 0.003	0.984 ± 0.013

High impedance MILOs, like the HMILO and S-MILO, may be inherently inefficient. Lower current MILOs produce less magnetic insulation, filling the AK gap with a larger electron hub when compared to more conventional MILOs that operate between 25 and 75 kA. This reduces the ability of electrons to transfer potential energy to the RF wave. Solutions to increasing the efficiency would be to operate at lower impedance/higher current, improve RF extraction, and reduce AK gap impurities.

For convenience, Table III tabulates the key experimental data from the three different datasets produced with the two experimental configurations. These tabulated parameters are extracted from the same data as the traces in Figs. 8 and 9. They will be used to compare with the theory in the next section.

VI. COMPARISON TO THEORY

Given the AK gap voltage V_a, input current I_a, and the anode and cathode radii r_a and r_c, the MILO operating point can be predicted using the Brillouin flow model [13]. The procedure is illustrated in detail for the MILO experiment in Packard et al. [11], who also applied the same procedure to several MILO experiments performed elsewhere [35], [36], [37], [38], [39]. The operating point in these experiments, relative to the BH condition, is also determined, once the phase velocity of the operating mode is given. We shall use the same procedure for the data points in our dual-frequency MILO experiments, assuming that operation at each frequency is independent of the other. The operating points for our dual-frequency MILO (see Table III) are shown in Fig. 11, along with the prior MILO experiments [11], [35], [36], [37], [38], [39].

Table IV presents a summary of relevant design and operating parameters for the MILO designs presented here, as well as the several MILOs treated by Packard et al. [11], Haworth et al. [35], Eastwood et al. [36], Cousin et al. [37], Yu-Wei et al. [38], and Min et al. [39]. The operating point of these experiments is shown in Fig. 11. It gives the degree of magnetic insulation [f, see (5)] in Fig. 11(b), or the amount of magnetic flux within the AK gap (A_a) in Fig. 11(a).

Note from Fig. 11 that our dual frequency MILO experiments operate much closer to the HC ($f = 1$) than the BH condition, and this trend is consistent with other MILO's, as observed by Packard et al. [11] and shown in Fig. 11.

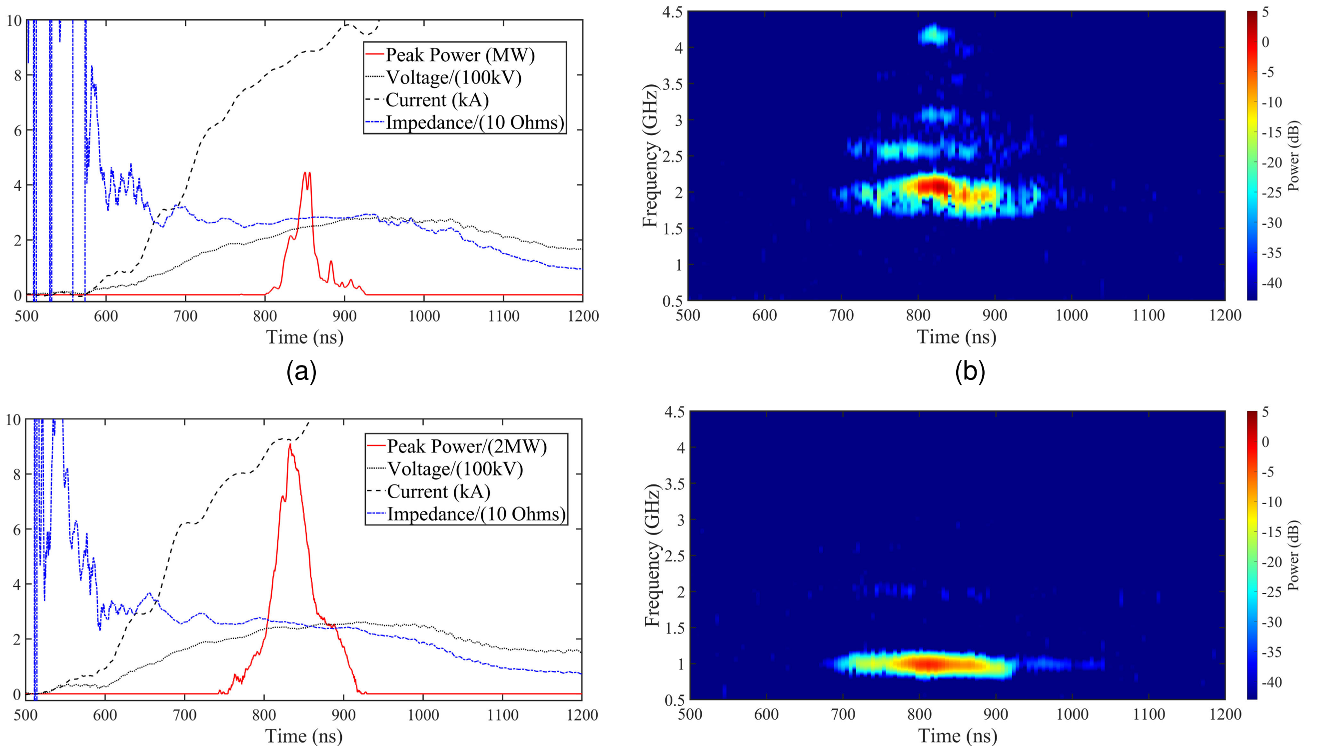

Fig. 9. Experimental HMILO data from shot 18 695 and shot 18 734. (a) Shot 18 695 data: voltage, current, power, and impedance; with maximum output power of 4.5 MW at 856 ns for HMILO-S. (b) Shot data 18 695: TFA of the RF signal with dominant frequency at 2.074 GHz. (c) Shot 18 734 data for HMILO-L with maximum output power of 18.2 MW at 833 ns. (d) Shot 18 734 data: TFA of the RF signal with dominant frequency at 0.985 GHz.

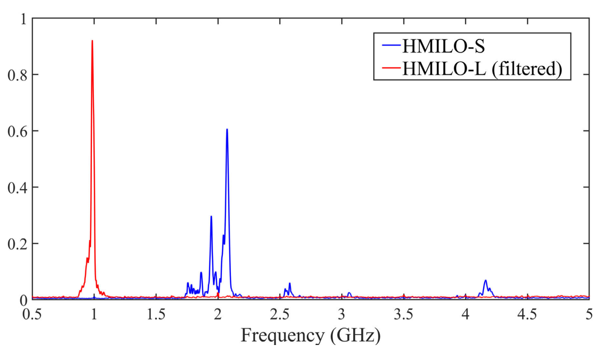

Fig. 10. Demonstration of harmonic dual-frequency MILO operation. Superimposed Fourier transforms from shot 18 695 and 18 734 with *S*- and *L*-bands extraction, respectively.

TABLE IV

OPERATING CONDITIONS OF EXPERIMENTAL MILOS FROM LITERATURE

Experiments and References	r_a (cm)	r_c (cm)	r_a/r_c	v_ph/c	V_a (kV)	I_a (kA)
S-MILO	2.5	0.8	3.125	0.286	207	7.3[1]
HMILO-S	2.5	0.8	3.125	0.286	238	8.6[2]
HMILO-L	2.5	0.8	3.125	0.286	256	9.9
Packard, [11]	2.5	0.7	3.57	0.286	256	9.1
Haworth, [35]	8.6	5.7	1.5	0.305	500	60
Eastwood, [36]	7.5	3.75	2	0.333	460	26
Cousin, [37]	4	2.5	1.6	0.281	400	30[3]
Fan, [38]	9.3	6.6	1.4	0.433	530	60
Min, [39]	7.28	4	1.82	0.385	520	37

[1] S-MILO requires 8.4 kA minimum current at 207 kV
[2] HMILO-S requires 9.2 kA minimum current at 238 kV
[3] Cousin's MILO requires 31.6 kA minimum current at 400 kV

The BH condition usually occurs at $f > f_u$, where f_u is a function of AK gap voltage only, and is given in [[11], Fig. 3(a)]. Physically, f_u is the value of magnetic insulation beyond which the anode current exceeds that required at HC ($f = 1$). The value of f at the BH condition is given in (10) of the Appendix. It is shown in Fig. 11(b) for various experiments [11], [35], [36], [37], [38], [39].

MILO has the peculiar property that it can achieve magnetic insulation at an anode current *lower* than that required at HC [13]. This occurs for $1 < f < f_u$. In this range of f, the minimum anode current to achieve magnetic insulation occurs at f_m, which depends only on the voltage V_a and is also shown in [[11], Fig. 3(a)].

Note that both f_u and f_m are also displayed in Fig. 11(a) and (b). A representative sample of MILOs illustrated in Fig. 11, with the exceptions of Haworth et al. [35], Cousin et al. [37], S-MILO, and HMILO-S are within the v-shaped curve in the range of $1 < f < f_u$, assuming $f > f_m$ placing the MILO operation on the right-hand side of the curve. Moreover, they operate with magnetic insulation less than BH [11].

Like Cousin's MILO, the S-MILO and HMILO-S experiments average operation did not achieve full magnetic insulation ($f < 1$). For the S-MILO at 207 kV, 7.3 kA was observed, while the required minimum current for magnetic insulation was 8.4 kA. Similarly, for the HMILO-S at 238 kV, 8.6 kA was observed and 9.2 kA was required for magnetic

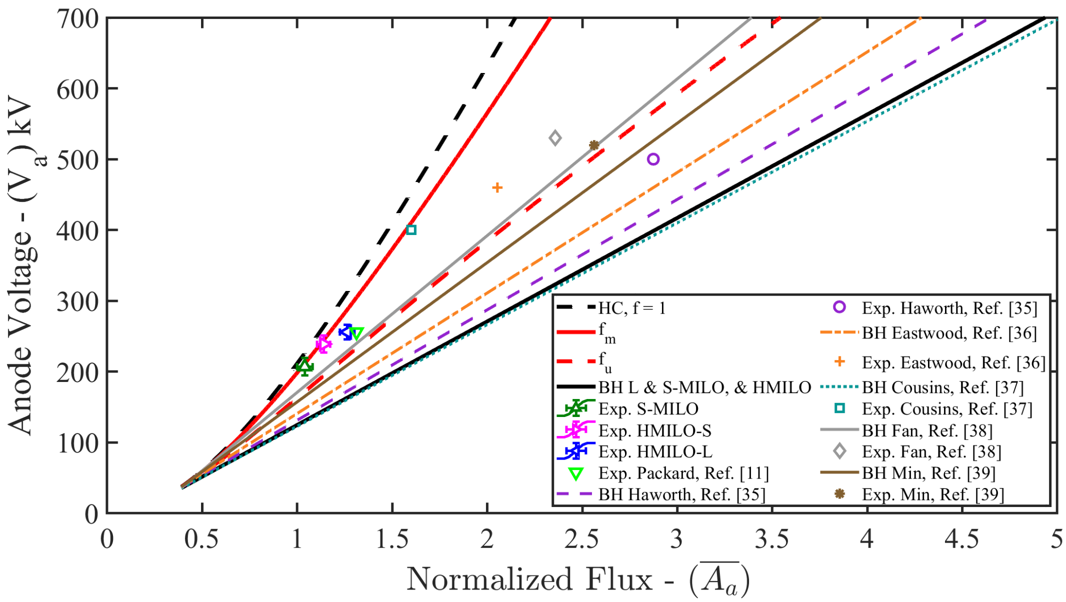

(a)

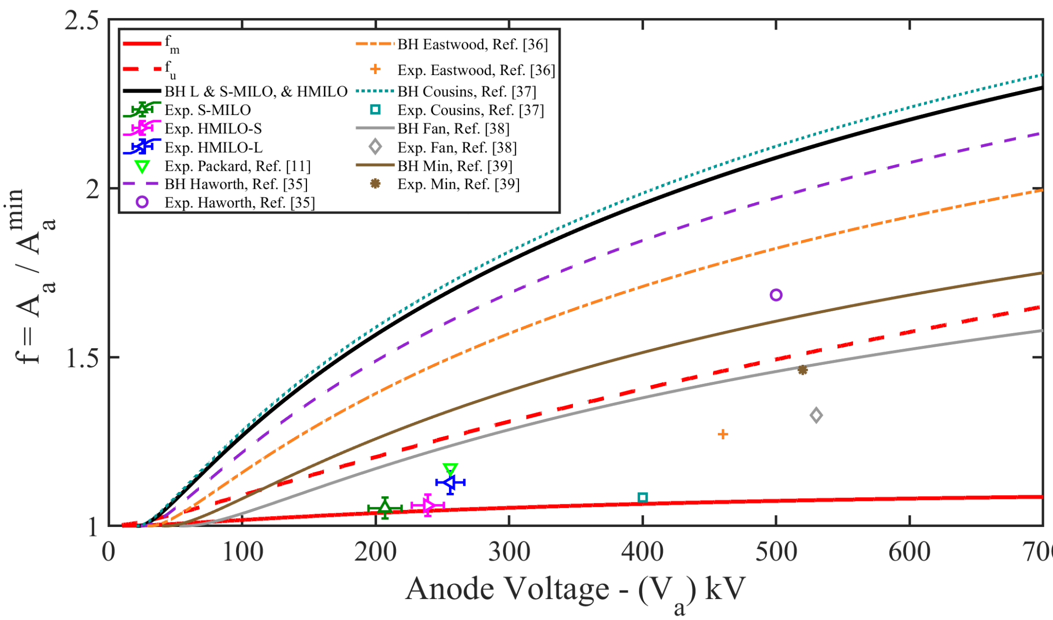

(b)

Fig. 11. Operating conditions of experimental MILOs throughout literature with each device's respective BH conditions. (a) Anode voltage (kV) versus normalized flux. (b) Magnetic flux ratio versus anode voltage (kV).

insulation. This places their operational points 10% below the theoretical minimum, f_m, as indicated in the footnote for Table IV. Consequently, this indicates the S-MILO and HMILO-S either oscillated without achieving complete magnetic insulation or barely achieved full insulation within the uncertainty bounds of the diagnostics utilized for the experiments. For these reasons, the S-MILO, HMILO-S, and the Cousin experiment intercept the f_m curve in Fig. 11, but theoretically they fall in the range $f < 1$. The HMILO-L did operate slightly beyond magnetic insulation, with parameters similar to Packard's L-MILO [11], as shown in Table IV and Fig. 11.

VII. Conclusion

Dual-frequency, harmonic oscillation at *L*-band (1 GHz) and *S*-band (2 GHz) was simulated and measured experimentally in a single MILO driven with a single driver, MELBA-C. Prior to the demonstration of the HMILO, an S-MILO, was also experimentally tested. The SWS of the S-MILO would subsequently become the *S*-band SWS of the HMILO. Brillouin flow theory was used for initial design and predictions of both S-MILO and HMILO behavior. Moreover, the novel theory agrees, within reasonable uncertainty, with the measured experimental behavior of the S-MILO and HMILO which operate at an anode current lower than that required for HC (for which $1 < f < f_u$ as shown in Fig. 11, or reside in the "v-shape curve" that is shown in [[13], Fig. 8(a)], and discussed extensively in [11]), like most other MILOs in the literature. Discrepancies between simulations and experimental output power are possibly due to plasma generation in the experiment, and dissimilar source pulse shapes. Future work could include the design of a high-power, coaxial directional coupler to make calibrated power measurements over the full frequency range in a single shot. Radiating the MILO output, possibly through a Vlasov antenna, and making a calibrated far-field measurement is a possibility. An additional measurement of the DSD current would provide insight into where the MILO lands on the v-shaped curve, specifically whether to right or left of f_m ($f < f_m$ or $f > f_m$) Also, work on novel radial extraction methods of the RF signal from a MILO could improve/modify packaging of the system.

Appendix
Degree of Magnetic Insulation (f) at BH Condition

This appendix presents a simple expression of the value of f, the degree of magnetic insulation defined in (5), when the BH condition is satisfied. This expression, given in (10) below, depends only on the phase velocity and on the gap voltage. It is independent of the mode and of the MILO geometry. Use of this expression readily shows that MILOs typically operate with a value of f much closer to HC than BH, as shown in Fig. 11.

The BH condition reads in our notation (see [[13], eq. (3.19)] or [[11], eq. (15)])

$$\bar{V}_a = \bar{A}_a \beta_{\text{ph}} + [\sqrt{1-\beta_{\text{ph}}^2} - 1] \tag{8}$$

where β_{ph} is the normalized phase velocity, v_{ph}/c. Equation (9) gives the value of $\bar{A}_a$ at BH

$$\bar{A}_a^{\text{BH}} = \frac{\gamma_a - \sqrt{1-\beta_{\text{ph}}^2}}{\beta_{\text{ph}}} = \frac{\gamma_a \gamma_{\text{ph}} - 1}{\gamma_{\text{ph}} \beta_{\text{ph}}} \tag{9}$$

where $\gamma_{\text{ph}} = 1/(1-\beta_{\text{ph}}^2)^{1/2}$ and γ_a is defined in (3) in terms of the gap voltage, V_a. The degree of magnetic insulation at BH, f^{BH}, follows from (4) and (5):

$$f^{\text{BH}} = \frac{\bar{A}_a^{\text{BH}}}{\bar{A}_a^{\text{min}}} = \frac{\gamma_a \gamma_{\text{ph}} - 1}{(\gamma_{\text{ph}} \beta_{\text{ph}})(\gamma_a \beta_a)}. \tag{10}$$

Note that f^{BH} depends only on the phase velocity (β_{ph}) and on the gap voltage (γ_a). Fig. 12 plots f^{BH} as a function of V_a at various values of β_{ph}.

We make the following remarks on the use of (8)–(10) for MILOs, and for magnetrons.

1) Equation (8) is valid in general, regardless of how the magnetic insulation is provided. It is applicable to magnetron, MILO, and their hybrid.
2) While (8) was derived from the Brillouin flow model for a cylindrical MILO, the same BH condition was obtained from the single particle model.
3) If a MILO operates with a high phase velocity, such as $\beta_{\text{ph}} \approx 0.6$, the Brillouin flow model is unreliable, because it implies a Brillouin hub extending significantly into the AK gap (in order that the electron velocity at the hub edge has a high value of β_{ph}), i.e., close to HC. All crossed-field flows close to HC are sensitive to small perturbation.
4) For $\beta_{\text{ph}} < 0.2$, operation at BH condition implies good magnetic insulation.

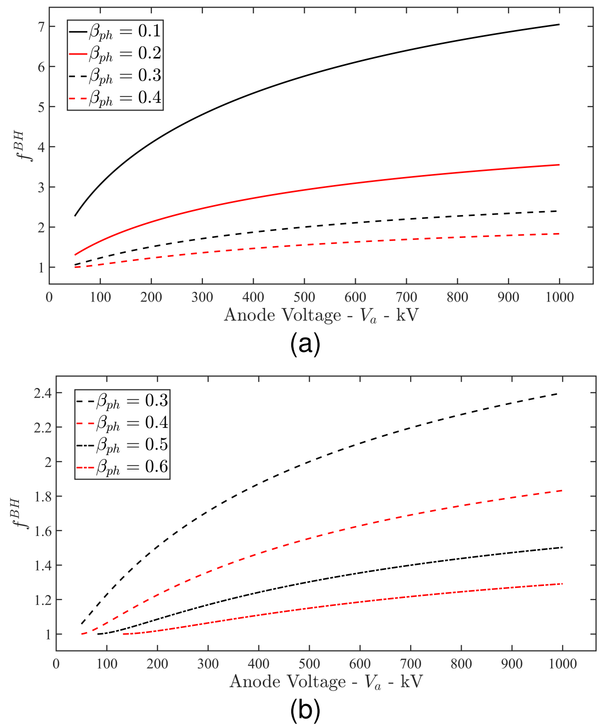

Fig. 12. Degree of magnetic insulation at BH condition, f^{BH}, as a function of V_a at various values of β_{ph}. (a) Traces for beta_ph at 0.1, 0.2, 0.3, and 0.4. (b) Traces for beta_ph at 0.3, 0.4, 0.5, and 0.6.

Since (8) and (9) are valid for MILO, magnetron, and their hybrid [13], (10) is applicable to them.

References

[1] M. Thumm, "Recent advances in the worldwide fusion gyrotron development," *IEEE Trans. Plasma Sci.*, vol. 42, no. 3, pp. 590–599, Mar. 2014.

[2] J. Benford, "Space applications of high-power microwaves," *IEEE Trans. Plasma Sci.*, vol. 36, no. 3, pp. 569–581, Jun. 2008.

[3] J. Benford and J. Swegle, "Applications of high power microwaves," in *Proc. 9th Int. Conf. High-Power Part. Beams*, vol. 1, May 1992, pp. 341–348.

[4] S. Min et al., "Analysis of electromagnetic pulse effects under high-power microwave sources," *IEEE Access*, vol. 9, pp. 136775–136791, 2021.

[5] D. Andreev, A. Kuskov, and E. Schamiloglu, "Review of the relativistic magnetron," *Matter Radiat. Extrem.*, vol. 4, no. 6, Nov. 2019, Art. no. 067201.

[6] A. W. Hull, "The effect of a uniform magnetic field on the motion of electrons between coaxial cylinders," *Phys. Rev.*, vol. 18, no. 1, pp. 31–57, Jul. 1921.

[7] S. Phelps, *The Tizard Mission: The Top-Secret Operation That Changed the Course of World War II*. Yardley, PA, USA: Westholme Publishing, May 2012.

[8] M. C. Clark, B. M. Marder, and L. D. Bacon, "Magnetically insulated transmission line oscillator," *Appl. Phys. Lett.*, vol. 52, no. 1, pp. 78–80, Jan. 1988.

[9] L. D. Bacon, W. P. Ballard, M. C. Clark, and B. M. Marder, "Magnetically insulated transmission line oscillator," U.S. Patent 4 785 261, Nov. 15, 1988.

[10] D.-B. Chen, D. Wang, F.-B. Meng, and Z.-K. Fan, "Bifrequency magnetically insulated transmission line oscillator," *IEEE Trans. Plasma Sci.*, vol. 37, no. 1, pp. 23–29, Jan. 2009.

[11] D. A. Packard et al., "Theory, simulation, and experiments on a magnetically insulated line oscillator (MILO) at 10 kA, 240 kV near hull cutoff condition," *Phys. Plasmas*, vol. 28, no. 12, Dec. 2021, Art. no. 123102.

[12] D. A. Packard et al., "Frequency and power measurements on the harmonic recirculating planar magnetron," *IEEE Trans. Plasma Sci.*, vol. 48, no. 6, pp. 1868–1878, Jun. 2020.

[13] Y. Y. Lau et al., "Explicit Brillouin flow solutions in magnetrons, magnetically insulated line oscillators, and radial magnetically insulated transmission lines," *IEEE Trans. Plasma Sci.*, vol. 49, no. 11, pp. 3418–3437, Nov. 2021.

[14] Z. Cendes, "The development of HFSS," in *Proc. USNC-URSI Radio Sci. Meeting*, Jun. 2016, pp. 39–40.

[15] M. C. Balk, "Simulation possibilities of vacuum electronic devices with CST PARTICLE STUDIO," in *Proc. IEEE Int. Vac. Electron. Conf.*, May 2008, pp. 459–460.

[16] R. E. Peterkin and J. W. Luginsland, "A virtual prototyping environment for directed-energy concepts," *Comput. Sci. Eng.*, vol. 4, no. 2, pp. 42–49, 2002.

[17] A. Palevsky, "Generation of intense microwave radiation by the relativistic e-beam magnetron (experiment and numerical simulation)," Ph.D. dissertation, Dept. Phys., Massachusetts Inst. Technol., Cambridge, MA, USA, 1980.

[18] B. McCowan, "Calculating slow-wave circuit parameters with HFSS," in *Proc. Abstr. Int. Vac. Electron. Conf.*, May 2002, p. 2.

[19] X. Gao et al., "Dispersion characteristics of a slow wave structure with metal photonic band gap cells," *Nucl. Instrum. Methods Phys. Res. Sect. A, Accel., Spectrometers, Detectors Associated Equip.*, vol. 592, no. 3, pp. 292–296, Jul. 2008.

[20] D. A. Packard et al., "HFSS and CST simulations of a GW-class MILO," *IEEE Trans. Plasma Sci.*, vol. 48, no. 6, pp. 1894–1901, Jun. 2020.

[21] G. B. Greening, N. M. Jordan, S. C. Exelby, D. H. Simon, Y. Y. Lau, and R. M. Gilgenbach, "Multi-frequency recirculating planar magnetrons," *Appl. Phys. Lett.*, vol. 109, no. 7, Aug. 2016, Art. no. 074101.

[22] R. Cousin, J. Larour, P. Gouard, and P. Raymond, "Evidence of the $3\pi/4$ interaction mode in a compact magnetically insulated line oscillator process," *J. Appl. Phys.*, vol. 100, no. 8, Oct. 2006, Art. no. 084512.

[23] J. W. Wang and G. A. Loew, "HEM_{11} modes revisited," in *Proc. Linear Accel. Conf.*, Albuquerque, NM, USA, 1990, pp. 135–137.

[24] W. Dong, C. Dai-Bing, Q. Fen, and F. Zhi-Kai, "Magnetically insulated transmission line oscillator oscillated in a modified HEM 11 mode," *Chin. Phys. B*, vol. 18, no. 10, pp. 4281–4286, Oct. 2009.

[25] D. Wang et al., "HEM_{11}mode magnetically insulated transmission line oscillator: Simulation and experiment," *Chin. Phys. B*, vol. 21, no. 8, Aug. 2012, Art. no. 084101.

[26] D. A. Packard, "Innovative crossed-field devices for the generation of high power microwaves," Ph.D. dissertation, Dept. Nucl. Eng. Radiol. Sci., Univ. Michigan, Ann Arbor, MI, USA, 2021.

[27] R. Collin, *Foundations for Microwave Engineering*. Hoboken, NJ, USA: Wiley, 2001.

[28] G. B. Collins, *Microwave Magnetrons*. New York, NY, USA: McGraw-Hill, 1948.

[29] D. M. Pozar, *Microwave Engineering*, 4th ed. Chichester, U.K.: Wiley, Nov. 2011.

[30] S. E. Calico, M. C. Clark, R. W. Lemke, and M. C. Scott, "Experimental and theoretical investigations of a magnetically insulated line oscillator (MILO)," *Proc. SPIE*, vol. 2557, pp. 50–59, Sep. 1995.

[31] A. D. Greenwood, "An ICEPIC convergence study using a relativistic magnetron," Directed Energy Directorate, Air Force Research Lab, Kirtland AFB, NM, USA, Tech. Rep. AFRL-DE-PSTM-2005-1005, May 2005.

[32] A. D. Andreev, S. M. Torrez, B. E. Nunan, and E. Schamiloglu, "Comprehensive particle-in-cell simulations of ten-vane microwave oven free-running 2.45 GHz 'cooker' magnetron with ICEPIC and CST-PS codes," *IEEE Trans. Plasma Sci.*, vol. 49, no. 11, pp. 3509–3518, Nov. 2021.

[33] M. R. López, "Experiments on a relativistic magnetron driven by a microsecond electron beam accelerator with a ceramic insulating stack," Ph.D. dissertation, Dept. Nucl. Eng. Radiol. Sci., Univ. Michigan, Ann Arbor, MI, USA, 2003.

[34] M. A. Franzi, "Relativistic recirculating planar magnetrons," Ph.D. dissertation, Dept. Nucl. Eng. Radiol. Sci., Univ. Michigan, Ann Arbor, MI, USA, 2014.

[35] M. D. Haworth et al., "Significant pulse-lengthening in a multigigawatt magnetically insulated transmission line oscillator," *IEEE Trans. Plasma Sci.*, vol. 26, no. 3, pp. 312–319, Jun. 1998.

[36] J. W. Eastwood, K. C. Hawkins, and M. P. Hook, "The tapered MILO," *IEEE Trans. Plasma Sci.*, vol. 26, no. 3, pp. 698–713, Jun. 1998.

[37] R. Cousin et al., "Gigawatt emission from a 2.4-GHz compact magnetically insulated line oscillator (MILO)," *IEEE Trans. Plasma Sci.*, vol. 35, no. 5, pp. 1467–1475, Oct. 2007.

[38] F. Yu-Wei et al., "A compact magnetically insulated line oscillator with new-type beam dump," *Chin. Phys. Lett.*, vol. 22, no. 1, pp. 164–167, Jan. 2005.

[39] S.-H. Min et al., "Characteristics of a transient axial mode from the formation of anode plasma in a gigawatt-class L-band magnetically insulated transmission line oscillator," *Phys. Plasmas*, vol. 23, no. 6, Jun. 2016, Art. no. 063120.

Ryan A. Revolinsky (Graduate Student Member, IEEE) received the B.S. degree in mechanical engineering, mechatronic engineering, and physics from California State University at Chico (CSUC), Chico, CA, USA, in 2021. He is currently pursuing the Ph.D. degree in nuclear engineering and radiological sciences with the University of Michigan, Ann Arbor, MI, USA.

He is currently with the Plasma, Pulsed Power, and Microwave Laboratory (PPPML), University of Michigan, where he conducts crossed-field high-power microwave research as a Graduate Student. He has completed an internship at the Laser Science and Engineering Operations (LSEO) Division, Lawrence Livermore National Laboratory (LLNL), Livermore, CA, USA, working on pulsed power, laser diodes, and controls. His research interests include magnetically insulated line oscillators (MILOs), recirculating planar magnetrons (RPMs), and crossed-field amplifiers. For this research, he applies theory, design, simulation, and experimentation skills to advance understanding of the above interests.

Emma N. Guerin (Graduate Student Member, IEEE) received the B.S.E. degree in nuclear engineering and radiological science from the University of Michigan, Ann Arbor, MI, USA, in 2021, where she is currently pursuing the Ph.D. degree in high-power microwave devices with the Plasma, Pulsed Power, and Microwave Laboratory.

She has been a Summer Intern at the Air Force Research Laboratory, Albuquerque, NM, USA.

Stephen V. Langellotti (Member, IEEE) received the B.S. degree in nuclear engineering from North Carolina State University, Raleigh, NC, USA, in 2017, and the M.S.E. and Ph.D. degrees in nuclear engineering and radiological sciences from the University of Michigan, Ann Arbor, MI, USA, in 2019 and 2022, respectively.

He is currently working as the Principle Physicist of Northrop Grumman, Rolling Meadows, IL, USA. He is also a former Reactor Operator for the PULSTAR nuclear reactor at North Carolina State University and was licensed by the U.S. Nuclear Regulatory Commission. His research interests include multipactor and high-power, high-frequency vacuum electronics.

Christopher J. Swenson (Graduate Student Member, IEEE) received the B.S.E. and M.S.E. degrees in nuclear engineering and radiological sciences from the University of Michigan, Ann Arbor, MI, USA, in 2018 and 2019, respectively, where he is currently pursuing the Ph.D. degree with the Plasma, Pulsed Power, and Microwave Laboratory.

His research interests include high-power microwave devices, including crossed-field amplifiers, magnetrons, and magnetically insulated line oscillators (MILOs).

Levi I. Welch (Student Member, IEEE) received the B.S. degree in nuclear engineering and radiological science from the University of Michigan, Ann Arbor, MI, USA, in 2021, where he is currently pursuing the M.S.E. degree.

He is currently with the Plasma, Pulsed Power, and Microwave Laboratory, University of Michigan, where he performs crossed-field high-power microwave research as a Graduate Student. He has participated as an Intern at the Plasma Physics Division, Naval Research Laboratory (NRL), Washington, DC, USA, working on GAMBLE II accelerator, an ion diode. His research interests include magnetically insulated line oscillators and recirculating planar magnetrons.

Drew A. Packard (Member, IEEE) received the B.S.E., M.S.E., and Ph.D. degrees in nuclear engineering and radiological sciences from the University of Michigan, Ann Arbor, MI, USA, in 2016, 2017, and 2021, respectively.

He is currently the Scientist of the Magnetic Fusion Energy Group, General Atomics, San Diego, CA, USA. In his undergraduate and graduate studies and as a Post-Doctoral Researcher with the Plasma, Pulsed Power, and Microwave Laboratory (PPPML), he has focused on high-power microwave source design and demonstration. He completed two internships with the Electron Devices Division, L-3 Communications, San Carlos, CA, USA, in 2015 and 2016. In his role at General Atomics, his research was focused on microwave heating for magnetically confined plasmas and accelerator development. His general research interests include charged particle beams, accelerators, diode physics, beam–wave interactions, RF sources and engineering, nuclear fusion, and microwave heating.

Nicholas M. Jordan (Senior Member, IEEE) received the B.S.E., M.S.E., and Ph.D. degrees in nuclear engineering and radiological science from the University of Michigan, Ann Arbor, MI, USA, in 2002, 2004, and 2008, respectively.

From 2008 to 2013, he was with Cybernet Systems, Ann Arbor, where he developed technology to disable uncooperative vehicles using microwave pulses. He is currently the Associate Research Professor of the Plasma, Pulsed Power, and Microwave Laboratory, University of Michigan. His current research interests include pulsed power, laser ablation, Z-pinch physics, plasma discharges, magnetrons, magnetically insulated line oscillators (MILOs), crossed-field amplifiers (CFAs), and other high-power microwave devices.

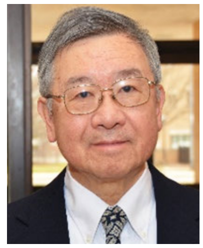

Y. Y. Lau (Fellow, IEEE) received the B.S., M.S., and Ph.D. degrees in electrical engineering from the Massachusetts Institute of Technology (MIT), Cambridge, MA, USA, in 1968, 1970, and 1973, respectively.

He was an Instructor and then an Assistant Professor of applied mathematics at MIT from 1973 to 1979; and a Research Physicist with Science Applications, Inc., McLean, VA, USA, from 1980 to 1983, and the U.S. Naval Research Laboratory, Washington, DC, USA, from 1983 to 1992. He has been a Professor with the University of Michigan, Ann Arbor, MI, USA, since 1992, where he became an Emeritus Professor in 2022. He has supervised or co-supervised 33 Ph.D. students. He has worked on electron beams, coherent radiation sources, plasmas, and discharges.

Dr. Lau was elected as a fellow of the American Physical Society in 1986. He was a recipient of the 1999 IEEE Plasma Science and Applications Award and the 2017 IEEE John R. Pierce Award for excellence in vacuum electronics. He has served three terms as an Associate Editor for *Physics of Plasmas* from 1994 to 2002.

Ronald M. Gilgenbach (Life Fellow, IEEE) received the B.S. and M.S. degrees from the University of Wisconsin–Madison, Madison, WI, USA, in 1972 and 1973, respectively, and the Ph.D. degree in electrical engineering from Columbia University, New York, NY, USA, in 1978.

In the mid-1970s, he spent several years as a Member of the Technical Staff at Bell Telephone Labs, Holmdel, NJ, USA. From 1978 to 1980, he performed gyrotron research at the Naval Research Laboratory (NRL), Washington, DC, USA, and conducted the first electron cyclotron heating experiments on a tokamak plasma at the Oak Ridge National Laboratory, Oak Ridge, TN, USA. He joined the University of Michigan (UM), Ann Arbor, MI, USA, in 1980, where he founded the Plasma, Pulsed Power and Microwave Laboratory and currently the Chihiro Kikuchi Collegiate Professor of the Nuclear Engineering and Radiological Sciences Department. He has served as the Department Chair of UM Nuclear Engineering and Radiological Sciences from 2010 to 2018. At UM, he has supervised or co-supervised 54 graduated Ph.D. students. He has more than 200 publications in refereed journals and book chapters and five U.S. patents. His research interests at UM include intense electron beams, high-power microwave generation, MA-LTD-driven z-pinches, laser ablation, and plasma diagnostics.

Dr. Gilgenbach is a fellow of the American Physical Society Division of Plasma Physics and the American Nuclear Society. He has received the 1997 IEEE Plasma Science and Applications Committee (PSAC) Award and the 2017 IEEE Peter Haas Pulsed Power Award. He has served as the IEEE PSAC Chair from 2007 to 2008. From 2017 to 2018, he has served on the National Academy of Sciences panel on a “Strategic Plan for U.S. Burning Plasma Research.” He has chaired the Review Committee for the Plasma Physics Division, Naval Research Laboratory (2013 and 2016) and served on the Advisory Board of Oak Ridge National Laboratories Nuclear Science and Technology Directorate (from 2013 to 2018). He is a past Associate Editor of the *Physics of Plasmas* journal.